

Crystallization of Lennard-Jones nanodroplets: From near melting to deeply supercooled

Shahrazad M. A. Malek, Gregory P. Morrow, and Ivan Saika-Voivod

Citation: *The Journal of Chemical Physics* **142**, 124506 (2015); doi: 10.1063/1.4915917

View online: <http://dx.doi.org/10.1063/1.4915917>

View Table of Contents: <http://scitation.aip.org/content/aip/journal/jcp/142/12?ver=pdfcov>

Published by the [AIP Publishing](#)

Articles you may be interested in

Molecular dynamics simulations of nucleation from vapor to solid composed of Lennard-Jones molecules
J. Chem. Phys. **134**, 204313 (2011); 10.1063/1.3593459

Origin of line tension for a Lennard-Jones nanodroplet

Phys. Fluids **23**, 022001 (2011); 10.1063/1.3546008

A thermodynamically consistent determination of surface tension of small Lennard-Jones clusters from simulation and theory

J. Chem. Phys. **133**, 044704 (2010); 10.1063/1.3456184

Nonequilibrium melting and crystallization of a model Lennard-Jones system

J. Chem. Phys. **120**, 11640 (2004); 10.1063/1.1755655

Critical cluster size and droplet nucleation rate from growth and decay simulations of Lennard-Jones clusters

J. Chem. Phys. **112**, 4193 (2000); 10.1063/1.480964



Crystallization of Lennard-Jones nanodroplets: From near melting to deeply supercooled

Shahrazad M. A. Malek, Gregory P. Morrow, and Ivan Saika-Voivod

Department of Physics and Physical Oceanography, Memorial University of Newfoundland, St. John's, Newfoundland and Labrador A1B 3X7, Canada

(Received 22 July 2014; accepted 4 March 2015; published online 27 March 2015)

We carry out molecular dynamics (MD) and Monte Carlo (MC) simulations to characterize nucleation in liquid clusters of 600 Lennard-Jones particles over a broad range of temperatures. We use the formalism of mean first-passage times to determine the rate and find that Classical Nucleation Theory (CNT) predicts the rate quite well, even when employing simple modelling of crystallite shape, chemical potential, surface tension, and particle attachment rate, down to the temperature where the droplet loses metastability and crystallization proceeds through growth-limited nucleation in an unequilibrated liquid. Below this crossover temperature, the nucleation rate is still predicted when MC simulations are used to directly calculate quantities required by CNT. Discrepancy in critical embryo sizes obtained from MD and MC arises when twinned structures with five-fold symmetry provide a competing free energy pathway out of the critical region. We find that crystallization begins with hcp-fcc stacked precritical nuclei and differentiation to various end structures occurs when these embryos become critical. We confirm that using the largest embryo in the system as a reaction coordinate is useful in determining the onset of growth-limited nucleation and show that it gives the same free energy barriers as the full cluster size distribution once the proper reference state is identified. We find that the bulk melting temperature controls the rate, even though the solid-liquid coexistence temperature for the droplet is significantly lower. The value of surface tension that renders close agreement between CNT and direct rate determination is significantly lower than what is expected for the bulk system. © 2015 AIP Publishing LLC. [<http://dx.doi.org/10.1063/1.4915917>]

I. INTRODUCTION

Nanotechnology has garnered much interest in the last few decades because of the wide range of applications that come out of it. Nanoclusters, small clusters comprising tens to millions of atoms, are used in a variety of settings, such as tuning the optical¹⁻³ and electronic properties of materials,^{2,4} biolabeling and imaging,⁵ catalysis,^{6,7} and chemical sensing.⁸ The various structures to which nanoclusters solidify, as well as their surface properties, bear a strong impact on their function.⁹

Much attention has been paid to the size dependence of nanocluster structure. Experimental work on argon clusters showed that for fewer than 50 atoms, polyicosahedral structure emerges,¹⁰ for larger particles up to 750 atoms multilayer icosahedra are formed, while beyond this size the structure becomes fcc.¹¹ Simulations with the Lennard-Jones (LJ) potential, a reasonable model for noble gases, as well as exhaustive searches of ground state structures confirmed this picture.¹²⁻¹⁴ LJ simulations generally reveal rather rich behavior, especially at finite temperature T , in terms of local and global structures, transformations, size dependence, and role of the surface.¹⁵⁻²⁴ Our interest is how various structures form out of the liquid state on cooling.

Freezing of a liquid generally occurs through the process of nucleation. This is accomplished when one of the embryonic crystallites that appear as structural fluctuations in the liquid reaches a sufficient size to overcome the crystal-liquid surface tension that tends to shrink and eliminate small crystalline

embryos. Classical Nucleation Theory (CNT) forms the basis of understanding the process qualitatively and provides quantitative predictions for the rate of nucleation. Central to CNT is $\Delta G(n)$, the reversible work required to form an embryo of size n particles of the stable phase within the metastable bulk.²⁵ However, the predicted rate is highly sensitive to this work, and therefore to such considerations as the shape of the embryos, the nature of the interface, and to the potentially T and curvature dependent surface tension.

The freezing of nanodroplets, i.e., nanoclusters in their liquid form, is complicated by the fact that such small systems can often freeze into more than one structure, for example icosahedral, decahedral or bulk-like fcc and hcp structures. Hence the nucleation process is potentially competitive in nanodroplets.²⁶ One wonders at what point during the freezing process does differentiation between structures occur and whether CNT provides a reasonable description of the rate at all. These are unresolved questions and their answers are likely system specific.

One study employing simulations of gold nanoparticles found that at sufficient supercooling, CNT predicted a constant or decreasing freezing rate with further supercooling while direct simulations saw the reverse, namely an increasing rate with further cooling.²⁷ This peculiar result is connected to broader questions regarding the choice of reaction coordinate in describing the nucleation process and the resulting free energy landscape, the description of nucleation when barriers are low, and the approach to a possible spinodal-like end to liquid

metastability.²⁸ Spinodal-like nucleation has been suggested to occur for bulk LJ,²⁹ but this idea has been challenged.^{30,31}

In the present study, we use molecular dynamics (MD) simulations to determine the freezing rate of a droplet consisting of 600 LJ particles. We press into service the mean first-passage time (MFPT) formalism of Reguera and co-workers^{32–34} to determine the rate and critical cluster sizes over a broad range of T . While generally for nanodroplets, the surface may play a large role in determining the rate, since a large fraction of particles is near or at the surface of the droplet, crystallization for the present system occurs within the interior.³⁵ We thus expect CNT as formulated for bulk liquids to hold without the modifications often employed to describe nucleation occurring on the surface.³⁶

The previous study of this system³⁵ also revealed that several competing structures, some based on fcc tetrahedra of different sizes, exist as basins within the free energy landscape of the system. However, as the free energy was calculated as a function of global measures of surface and bulk crystallinity, little light was shed on the question of how these different structures arise.

This paper is organized as follows. In Sec. II, we review and discuss some aspects of CNT and MFPT, while we provide details of our simulations in Sec. III. We report our results in Sec. IV, including a determination of the liquid-solid coexistence temperature, the freezing rate as a function of T from MD simulations, modelling the T dependence of the rate through CNT, determining the free energy of crystallite formation, and an analysis of critical nuclei structure. Section V provides a discussion of our results before summarizing our conclusions in Sec. VI.

II. CNT, MFPT AND THE LOW BARRIER REGIME

A. CNT

According to CNT,^{25,37} the rate of nucleation J , that is to say the number of crystalline embryos that cross the critical size threshold and start to grow per unit time in the steady-state, is given by

$$J_{\text{CNT}} = N_p Z f_{\text{crit}}^+ \exp(-\beta \Delta G^*), \quad (1)$$

where N_p is the number of molecules in the system, the Zeldovich factor is $Z = \left(\frac{\beta}{2\pi} \left| \frac{\partial^2 \Delta G(n^*)}{\partial n^2} \right| \right)^{1/2}$, $\beta = (k_B T)^{-1}$ with k_B the Boltzmann constant, $\Delta G^* = \Delta G(n^*)$, the minimum work required to form an embryo of critical size n^* , and f_{crit}^+ is the attachment rate of molecules to an embryo of size n^* . We note that, at variance with Eq. (1), the rate is often stated in terms of the number of nucleation events per unit time per unit volume. Here, we have absorbed the volume of the system into J_{CNT} .

The reversible work required to assemble an embryo of size n is related to the distribution of embryo sizes in the system³⁷

$$\beta \Delta G(n) = -\ln \left[\frac{N(n)}{N_t} \right] \approx -\ln \left[\frac{N(n)}{N_p} \right], \quad (2)$$

where $N(n)$ is the equilibrium number of embryos of size n in the system and $N_t = \sum_{i=0}^h N(i)$ is the total number of

embryos (including liquid-like particles) in the system and is approximated by N_p since we assume that the system is dominated by liquid-like particles, and h is a constraint on the largest embryo size that is necessary to formally define the metastable equilibrium state. $N(0)$ refers to the number of liquid-like particles in the system, while $N(1)$ refers to the number of particles that are themselves crystal-like, but the neighbor of which are liquid-like. Because of surface tension γ between liquid and crystal, $\Delta G(n)$ is initially positively sloped and possesses a maximum at n^* .

The simplest model for the work of crystallite formation is^{25,37}

$$\beta \Delta G(n) = -\beta \Delta \mu n + \beta \gamma A n^{2/3}, \quad (3)$$

where $\Delta \mu = \mu_L - \mu_S$ is the difference between the chemical potentials for the bulk phase μ_L and the embryo phase μ_S , with $\Delta \mu > 0$, and A is a shape-dependent proportionality constant that assumes that embryos are compact, i.e., for an embryo of volume $\sim n$, the surface area should be $S = An^{2/3}$. For spherical embryos, $A = \sqrt[3]{36\pi v^2}$, where v is the volume per particle in the embryonic phase. Within this model, $\beta \Delta G^* = \frac{4}{27} \frac{(\beta A \gamma)^3}{(\beta \Delta \mu)^2}$, $n^* = \frac{8}{27} \frac{(\beta A \gamma)^3}{(\beta \Delta \mu)^3}$, and $Z = \frac{3}{4\sqrt{\pi}} \frac{(\beta \Delta \mu)^2}{(\beta A \gamma)^{3/2}}$.

The simplest model for the T -dependence of J_{CNT} is obtained by combining Eqs. (1) and (3), along with assuming γ and A constant. By further assuming a constant enthalpy difference ΔH between the liquid and crystal phases as T decreases at constant pressure p , one obtains

$$\beta \Delta \mu = \frac{\Delta H}{N_p k_B} \frac{T_m - T}{T T_m}, \quad (4)$$

where T_m is the melting temperature of the bulk crystal, and at which point J_{CNT} is zero. Additionally, one assumes a simple Arrhenius T dependence of the critical attachment rate

$$f_{\text{crit}}^+ = f_0 \exp\left(-\frac{C}{T}\right), \quad (5)$$

where $k_B C$ is an activation free energy. Combining all these approximations results in^{38,39}

$$J_{\text{CNT}}(T) = \lambda \frac{(T_m - T)^2}{\sqrt{T}} \exp\left[-\frac{C}{T} - \frac{B}{T(T_m - T)^2}\right], \quad (6)$$

which predicts a maximum rate to occur even in the absence of considerable slowing down of dynamics. The simple modelling employed implies that the barrier to nucleation is

$$\beta \Delta G^* = \frac{B}{T(T_m - T)^2}, \quad (7)$$

and therefore has a minimum at $T_m/3$, which tends to maximize the rate, before diverging as T approaches zero. In terms of the physical quantities ΔH , T_m , f_0 , A , and γ , the parameters λ and B in the model are given by

$$\lambda = f_0 N_p \frac{3}{4\sqrt{\pi} k_B} \frac{1}{(A \gamma)^{3/2}} \left(\frac{\Delta H}{N_p} \right)^2 \frac{1}{T_m^2}, \quad (8)$$

$$B = \frac{4}{27} \frac{(A \gamma)^3}{k_B} \left(\frac{N_p}{\Delta H} \right)^2 T_m^2. \quad (9)$$

The quantities λ , T_m , B , and C can, in principal, be obtained through fitting the rate as a function of T with Eq. (6).

B. n_{\max} as the order parameter

In the present work, as is now common in simulation studies of nucleation, we employ the size of the largest embryo in the system n_{\max} as a reaction coordinate. Once an embryo definition is set, every system configuration can be uniquely assigned a value of n_{\max} , and hence the configurational part of a restricted partition function can be defined through²⁷

$$Q(n_{\max}) = \sum_{c \in n_{\max}} \exp(-\beta U_c), \quad (10)$$

where U_c is the potential energy of configuration c , restricted to those configurations that have a largest embryo of size n_{\max} . We can then further define the free energy⁴⁰

$$\beta \Delta F(n) = -\ln \left[\frac{Q(n)}{Q_{\text{liq}}} \right], \quad (11)$$

where we have dropped the subscript on n for notational convenience and Q_{liq} is the partition function of the metastable liquid, defined as

$$Q_{\text{liq}} = \sum_{n=0}^{n_F^*} Q(n), \quad (12)$$

where n_F^* is the (critical) cluster size at which $\beta \Delta F(n)$ possesses a local maximum, i.e., where $Q(n)$ has a local minimum. So defined, $\beta \Delta F(n)$ is directly related to the probability that the largest cluster in the system is of size n , given that the system is in the metastable liquid, $P_{\max}(n)$,

$$\beta \Delta F(n) = -\ln P_{\max}(n). \quad (13)$$

That is, the normalization is such that

$$\sum_{n=0}^{n_F^*} P_{\max}(n) = 1. \quad (14)$$

For relatively large barrier heights, large embryos are rare, i.e., there is only one large embryo in the system if there is one at all. This implies the equality of the following three quantities: the probability of there being an embryo of size n in the system; the probability that the largest embryo is of size n ; and the average number of embryos of size n . This becomes immediately obvious when constructing related histograms during the simulations. In this regime, $P_{\max}(n) = N(n)$ (and both are small).

The transition state theory (TST) rate expression when there is a free energy barrier present is

$$J_{\text{TST}} = f^+(n_F^*) Z_F \exp[-\beta \Delta F^*], \quad (15)$$

where n_F^* , the Zeldovich factor $Z_F = [\beta \Delta F''(n_F^*)/(2\pi)]^{1/2}$ and $f^+(n_F^*)$, the generalized diffusion coefficient at the critical state, become equal to n^* , Z , and f_{crit}^+ at sufficiently high barriers, respectively, and $\beta \Delta F^* = \beta \Delta F(n_F^*)$. f_{crit}^+ in Eq. (1) is the attachment rate of particles to an embryo of critical size, while $f^+(n_F^*)$ tracks changes in the size of the largest embryo at critical size in the system. The two are the same so long as the largest embryo in the system is the only embryo near the critical size. Again, when barriers are high, the equalities $n^* = n_F^*$ and $P_{\max}(n) = N(n)$ near n^* imply that $\beta \Delta G^* = \beta \Delta F^* + \ln N_p$, and this is consistent when comparing Eqs. (1) and (15). However,

there is no reason why this should hold when barriers become low.

It is generally the case that $\Delta F(n)$ possesses a minimum at n_{\min} , the most likely largest embryo size. It is tempting to formulate Eq. (15) in terms of the free energy difference

$$\beta \Delta F_{\min}^* = -\ln \left[\frac{P_{\max}(n_F^*)}{P_{\max}(n_{\min})} \right] = \beta \Delta F^* - \beta \Delta F(n_{\min}). \quad (16)$$

This is incorrect in terms of rate prediction, as it fails to account for the phase space available in the free energy basin around n_{\min} .⁴⁰

The identification of $\Delta F_{\min}^* \rightarrow 0$ with a spinodal has been shown to be incorrect,³⁰ but it nonetheless marks the point at which the liquid system ceases to possess a basin in the free energy and has therefore lost formal metastability. For bulk systems of finite size, this marks the point at which phase change proceeds through the monotonic increase in size of the largest embryo in the system with time, i.e., because the system is large enough, it becomes probable that it possesses an embryo of critical size as soon as diffusive particle attachment allows. Phase transformation of the sample thus proceeds through growth-limited nucleation.³⁴ However, the metastable phase has not lost inherent metastability as work is still required to form an embryo. For systems such as our nanodroplets, it is perhaps not meaningful to distinguish between phase and system, but we nonetheless expect that the loss of metastability occurring at $\Delta F_{\min}^* = 0$ to be actualized through a growth-limited nucleation mechanism with a transformation rate given, at least approximately, by Eq. (1). A true kinetic spinodal, i.e., a loss of stability on the particle level, should occur when ΔG^* vanishes.

C. MFPT

In recent times, Reguera and co-workers reformulated the use of mean first-passage time from TST^{32-34,41} in order to characterize the nucleation process in the regime where nucleation times are accessible by direct MD simulations. In this MFPT formalism, when the time to crystallize is dominated by barrier crossing, the mean time at which the largest crystalline embryo in the system first reaches size n is given by

$$\tau(n) = \frac{\tau_J}{2} \{1 + \text{erf}[Z_F \sqrt{\pi}(n - n_F^*)]\}, \quad (17)$$

where $\tau_J = 1/J$. Thus, calculating $\tau(n)$ from an ensemble of simulations for which crystallization takes place yields good estimates of J as well as Z and n^* .

Typically, as supercooling increases, the sigmoidal shape of the MFPT becomes less well described by Eq. (17), and we can instead estimate n_F^* through³²

$$\frac{\partial^2 \tau(n_F^*)}{\partial n^2} \approx 0. \quad (18)$$

III. MODEL AND SIMULATIONS

Our system consists of $N_p = 600$ particles interacting through the LJ pair potential, $U_{LJ}(r) = 4\epsilon \left[\left(\frac{\sigma}{r}\right)^{12} - \left(\frac{\sigma}{r}\right)^6 \right]$,

simulated in the canonical ensemble. All reported quantities are given in reduced dimensionless units, e.g., length is rescaled by σ , energy by ϵ , time by $\sqrt{\epsilon/(m\sigma^2)}$ (where m is the mass of a particle), temperature by ϵ/k_B , and pressure by ϵ/σ^3 . We use a cubic simulation box of side length $L = 30$ and employ a potential cutoff of $R_c = 14.99999$. For the range of T we consider, the system consists of a single condensed droplet with a few particles at most detaching themselves from the droplet into the surrounding gas phase. The finite size and periodic boundaries ensure that these particles can return to the droplet and that the droplet does not evaporate. The box size is sufficiently large to ensure that particles within the droplet do not interact unphysically with periodic images of the droplet.

We use Gromacs v4.5.5⁴² to carry out MD simulations. Temperature is maintained with the Nosé-Hoover thermostat with a time constant of 1. We use a time step of $\Delta t = 0.001$ and integrate equations of motion with the leap-frog algorithm. We equilibrate the system at $T = 0.53$, for which the droplet is well formed but clearly a liquid and subsequently harvest 501 independent configurations by sampling every 100 000 time steps. Each of these configurations serves as a starting point for a “crystallization run,” for which the thermostat is set to the desired lower T . We determine $\tau(n)$ from the MFPT formalism, as in Refs. 32 and 43 from these 501 crystallization trajectories for each of several T from 0.490 down to 0.385 in steps of 0.005, and from 0.350 to 0.100 in steps of 0.05. To determine $\tau(n)$, we calculate the size of the largest crystalline embryo, as described below, every 1000 time steps (integer LJ time units).

We employ the procedure developed by Frenkel and co-workers^{44,45} to define crystal-like embryos within the droplet, based on quantifying the local bond ordering for a single particle via spherical harmonics.⁴⁶ See also Refs. 43 and 47 for details. In this procedure, there are three parameters: the distance cutoff for determining whether two particles are neighbors, chosen from the minimum at $r = 1.363$ between first and second peaks of the radial distribution function; a threshold for the correlation c_{ij} , a complex dot product that determines whether two neighboring particles have sufficiently aligned local bonding patterns and above which the particles are considered to be *connected*, which we choose to be 0.5 as the intersection point for the probability distributions of c_{ij} obtained from 100 liquid and 100 solidified configurations at $T = 0.475$; and the number of connections a particle needs in order to be considered solid-like, which we take to be 0.8 times the number of neighbors a particles has (keeping in mind that particles on the surface have fewer neighbors). Further, for the purposes of finding the size distribution of embryos, two connected, crystal-like particles are considered to be part of the same crystalline embryo.

In order to differentiate between embryos of the same size but different overall structures, we determine the overall crystallinity of the cluster by calculating the often-used quantity Q_6 .⁴⁸

To determine the free energy profiles, we carry out umbrella sampling Monte Carlo (MC) simulations in the canonical ensemble to determine the works defined in Eqs. (2) and (13). When barriers are reasonably high, we make use of a biasing potential,

$$\phi(n_{\max}) = \frac{1}{2}\kappa(n_{\max} - n_0)^2, \quad (19)$$

where $\kappa = 0.00625$ determines the strength of the constraint and n_0 is the target embryo size. Following the method in Refs. 30, 43, 44, and 47, the MC procedure consists of first noting at iteration step i , the value of the constraint for a configuration o , ϕ_o , and then generating an unbiased MC trajectory in the canonical ensemble with the Metropolis algorithm for 10 displacement attempts per particle to arrive at a new configuration w with a value of the constraint potential ϕ_w . The new configuration is accepted (w becomes the configuration at iteration $i + 1$) with probability $\min[1, \exp(\beta\phi_o - \beta\phi_w)]$. Otherwise, o remains the configuration at iteration $i + 1$.

We carry out biased simulations for several values of n_0 for each T and correct for the bias in determining portions of $N(n)$ and $P_{\max}(n)$ around each n_0 according to Ref. 44. As in Ref. 47, we discard histogram bins with poor statistics and simply shift the different portions of $\beta\Delta F(n)$ and $\beta\Delta G(n)$ to minimize the difference in the range of n for which the pieces overlap. We check our procedure with MBAR⁴⁹ and our results agree to within the error. $\beta\Delta F(n)$ is normalized according to Eq. (14) and for $\beta\Delta G(n)$, we determine N_t so that $\exp[-\beta\Delta G(0)] + \sum_{i=1}^{n^*} \exp[-\beta\Delta G(i)] = N_p$. This latter condition is usually indistinguishable to within $0.1k_B T$ from imposing the condition $\beta\Delta G(0) = 0$ in terms of determining $\beta\Delta G^*$.

When the barrier is sufficiently low, we impose a simple “hard wall” constraint, namely, that any MC trajectory that results in $n_{\max} > n_0$ is rejected, using only a single n_0 for a given T . When using a hard wall constraint, it is important to not place it much beyond the critical embryo size. A good check is that the time series of n_{\max} should not get “stuck” near the constraint. If the constraint is too large, poor sampling will result in an apparent barrier height and critical size that are both too large. In both biasing schemes, we generally use 20 independent starting configurations in order to obtain good averages.

IV. RESULTS

A. The melting temperature

There are two melting temperatures to speak of. According to Eq. (3), the barrier to nucleation becomes infinite and the rate is zero at T_m , when $\Delta\mu = 0$, i.e., the melting temperature in the thermodynamic limit. For bulk LJ at $p = 0$, this is the fcc melting temperature of 0.618.⁵⁰ For comparison, the pressure of our system, evaluated from the virial as for a bulk system, is less than 10^{-4} , effectively zero. Thus, $T_m = 0.618$ is a reasonable estimate.

However, for our finite-sized cluster, the presence of a surface complicates matters and the coexistence temperature should be defined as the temperature at which the droplet as a whole has equal probability of being either in the solid or liquid state. To determine this temperature, we note that the system at $T = 0.490$ is predominantly in the liquid state but makes short excursions to being largely solid (a surface melted state). This flipping between states is readily apparent in any of the 501 potential energy time series

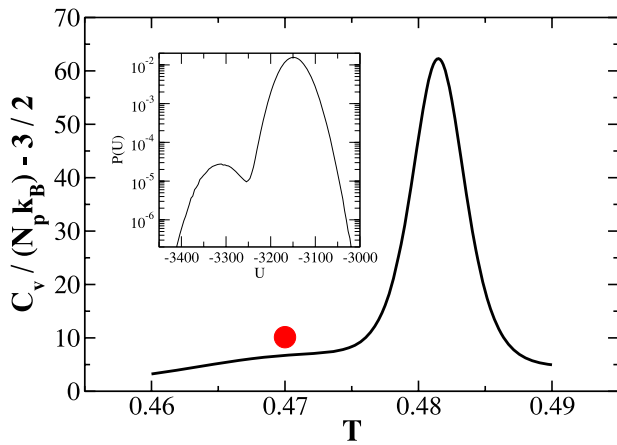


FIG. 1. Heat capacity as a function of T . $C_V(T)$ is determined by reweighting the double-peaked potential energy probability distribution $P(U)$ at $T = 0.490$ shown in the inset. The peak at $T = 0.482$ marks the coexistence temperature between liquid and solid cluster states. The circle is the value of C_V at $T = 0.470$ determined from solidified cluster states.

we have collected (not shown). From these time series, we construct the probability distribution for the potential energy $P(U)$, which has a distinctly bimodal character as shown in the inset of Fig. 1. The main part of the figure shows the heat capacity $C_V(T)$ extrapolated through straightforward temperature reweighting of $P(U)$. Also plotted is a point for $C_V(T = 0.470)$, as determined solely from energy fluctuations in the crystallized state at that T . That the discrepancy is small at $T = 0.470$ allows us to estimate the coexistence temperature for our cluster to be $T_m^c = 0.482$. Clearly, T_m^c is not the intended melting temperature in Eq. (6).

B. Nucleation rates from MFPT

Prior to determining the rate, we consider the potential energy per particle U/N_p as a function of time after the quench from $T = 0.530$ to the various target temperatures. At low to moderate supercooling, e.g., from $T = 0.485$ to $T = 0.430$ in Fig. 2(a), the initial rapid change in U shows the system reaching a metastable equilibrium, where the droplet is liquid. The sharp drop in U for these T , after metastable equilibrium is achieved, marks rapid growth of a postcritical crystalline embryo, as evidenced by the commensurate sharp increase in

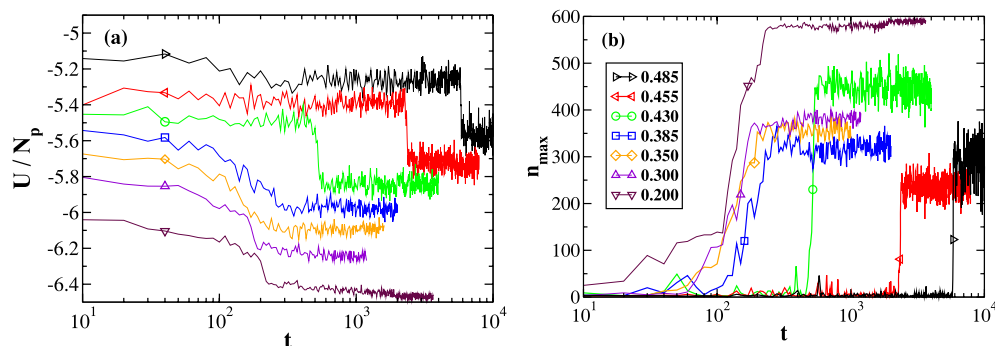


FIG. 2. Time series of (a) potential energy U and (b) largest embryo size n_{\max} showing crystallization events. At higher T , the nearly vertical changes in the graphs indicate very fast growth compared to the lifetime of the metastable liquid state. Legend indicates T for both panels. At $T = 0.385$, the metastable state becomes difficult to discern. At $T = 0.200$, the system progresses essentially monotonically to the frozen state.

n_{\max} in Fig. 2(b). At $T = 0.385$, the metastable state is less clearly seen, if at all, near $t = 60$ and the decrease in U beyond $t \approx 90$ is accompanied by an increase in n_{\max} . By $T = 0.200$, the system proceeds monotonically from the $T = 0.530$ state, with both U and n_{\max} sliding towards the frozen state. The sharp change in U and n_{\max} near $t = 200$ occurs after most of the droplet is already crystalline. While this is interesting, we do not consider it in this study.

Next, we wish to quantify the rate of nucleation from $\tau(n)$. A sampling of curves from our range of T is shown in Fig. 3, where we have normalized the curves by $\tau(n = 250)$ since nucleation times vary widely. We define a crystallization rate as $J_{250} \equiv 1/\tau(250)$ that should approximately equal the nucleation rate at shallow supercooling, but clearly underestimate the nucleation rate at low T as it captures much time spent by a post-critical embryo growing to a size of 250.

At shallow to moderate supercooling, $\tau(n)$ is fairly well approximated by Eq. (17). We thus define $J_{\text{MFPT}} \equiv 1/\tau_J$, where τ_J is determined from fitting to Eq. (17) for $T = 0.415$ and higher. From the fit, we also obtain n_{MFPT}^* as an estimate for n_F^* .

In order to extend the determination of the nucleation rate to lower T , we find the inflection point in $\tau(n)$ and so define n_{inf}^* according to Eq. (18). Since the system has equal probability of growing or shrinking at n_F^* , we define another estimate of the nucleation rate $J_{n^*} \equiv 1/[2\tau(n_{\text{inf}}^*)]$. We plot n_{MFPT}^* and n_{inf}^* in Fig. 9(b).

The progression of the change of shape of $\tau(n)$ upon lowering T is noteworthy. At first, the low- n plateau shrinks as n_F^* decreases. Along with this, the steepness of $\tau(n)$ for small n increases. However, below $T \approx 0.4$, the curves become progressively less steep, and by $T = 0.250$, the inflection clearly occurs at larger n . An increase in n^* on lowering T is not predicted by CNT but rather is predicted by mean field theories of spinodal-type nucleation. While this warrants further investigation, we note that there are likely strong non-equilibrium effects at this very low T .

We show the temperature dependence of our three rates J_{250} , J_{MFPT} , and J_{n^*} in Fig. 4. All three rates agree from high T down to 0.415, the lowest T at which we determine J_{MFPT} . Below this T , the difference in J_{250} and J_{n^*} reflects the lack of separation of growth and nucleation time scales. Both J_{250} and J_{n^*} exhibit a broad maximum and show only a weak T dependence below $T = 0.4$.

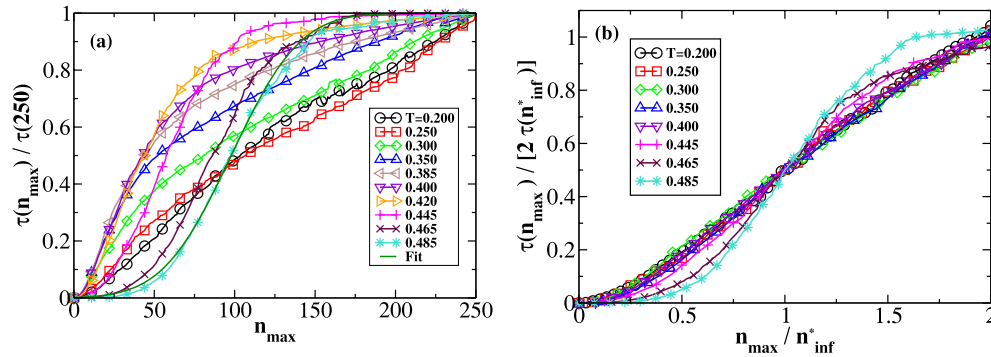


FIG. 3. Mean first-passage time $\tau(n_{\max})$ for the appearance of an embryo of size n_{\max} for a range of T indicated by the legend. In (a), curves are normalized by $\tau(250)$. For $T = 0.485$, we show a fit according to Eq. (17). This sigmoidal shape is progressively lost with increased supercooling as the early time plateau shortens. Below $T = 0.35$, curves become less steep at small n_{\max} , which tends to move the inflection point to larger n_{\max} , and the curves become more linear. In (b), we plot the data rescaled with n_{inf}^* , the inflection point.

In Sec. IV C, we determine the extent to which simple CNT can quantitatively account for the T dependence of the rate.

C. T dependence of the rate from CNT

As discussed in Sec. II A, the simplest model for $J(T)$ assumes an Arrhenius dependence of the attachment rate on T , a constant surface tension, and a constant difference in enthalpy between the solid and liquid phases. The resulting model is given in Eq. (6). We use it to fit J_{250} and J_{MFPT} . J_{250} is a crystallization rate blind to the separation of nucleation and growth time scales and should not yield good results. By contrast, J_{MFPT} represents a T range for which nucleation and growth are well separated.

Given the orders-of-magnitude difference in the rates as T varies, we fit by first taking logarithms of both sides of Eq. (6). The resulting fits of J_{250} and J_{MFPT} are plotted in Fig. 4(a), and the fit parameters are as follows. For J_{250} (fitting from $T = 0.200$ to 0.485): $\lambda = 87$, $T_m = 0.54$, $B = 1.5 \times 10^{-2}$, $C = 1.7$. For J_{MFPT} (fitting from 0.415 to 0.485): $\lambda = 2.8 \times 10^{21}$, $T_m = 0.67$, $B = 0.54$, $C = 14$. Choosing data from J_{250} in the same temperature range over which J_{MFPT} is calculated produces similar fit parameters to those for J_{MFPT} . The fits for J_{MFPT} are more stable with respect to data sampling. Thus, the parameters vary widely according how much of the data below $T \approx 0.43$ is taken for fitting. Unfortunately, fitting yields physically unrealistic or imprecise parameters.

So while as a fitting function Eq. (6) is able to reproduce the T dependence of the rate, it is difficult to extract meaningful physical quantities from the fits parameters. Our goal is therefore to reduce the fit parameters to just γ by independently determining T_m , ΔH , A , f_0 , and C .

1. The enthalpy difference

The enthalpy difference $\Delta H = U_L - U_S + P(V_L - V_S)$ between solid and liquid enters into the coefficients of Eq. (6). Given that our system is at a very small pressure, that the densities of liquid and crystal are comparable and that there is a sizeable potential energy difference between liquid and crystal, we approximate $\Delta H \approx U_L - U_S \equiv N_p \Delta u$, where Δu is the per particle potential energy difference between the liquid and crystal. The scenario is complicated here by the fact that when our droplet solidifies, it does so incompletely and remains partially liquid. Calling ΔU the difference in potential energy between the liquid and (partially) solidified droplet, and α the fraction of particles in the solidified droplet identified as solid-like, then we can estimate the enthalpy difference as

$$\frac{\Delta H}{N_p} = \Delta u = \frac{1}{\alpha} \frac{\Delta U}{N_p}. \quad (20)$$

In the inset of Fig. 5, we plot α as a function of T , and see that the fraction of solid-like particles in the frozen state, at least according to our order parameters, increases roughly linearly with decreasing T . In the main panel of Fig. 5, we plot

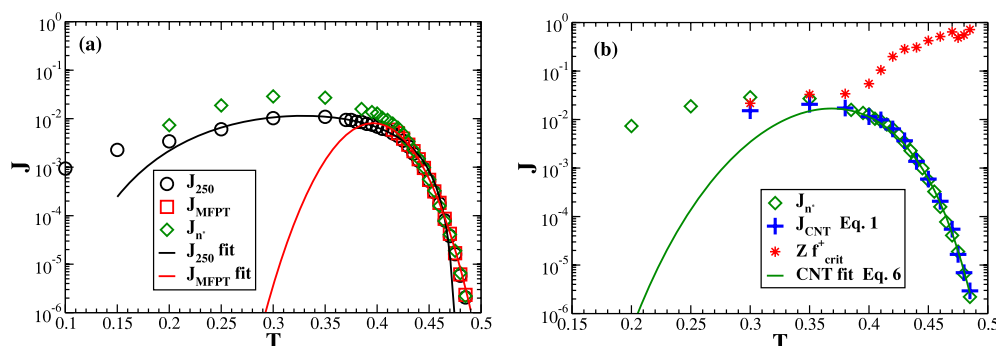


FIG. 4. Nucleation rate as a function of T . Panel (a) shows three estimates as described in the text of J based on $\tau(n)$, which all agree at higher T . Curves are fits according to Eq. (6). Panel (b) shows a comparison of $J_n(T)$ with the rate predicted by Eq. (1) (plus signs) and a one-parameter fit to obtain $\gamma = 0.128$ using Eq. (6) (curve) with other parameters determined independently. Also shown is the kinetic prefactor (stars) of Eq. (1).

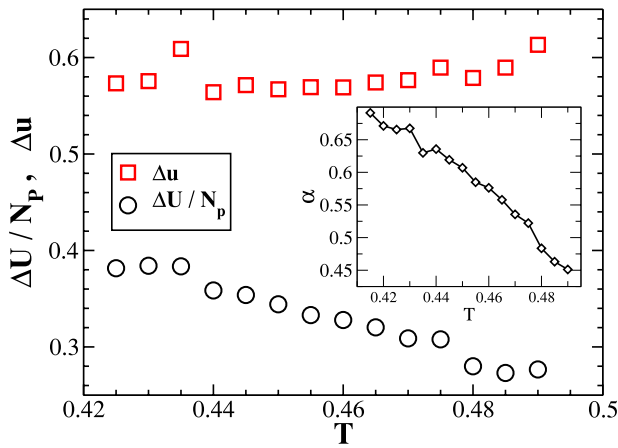


FIG. 5. Determining $\Delta H/N_p$. Circles show the raw estimate $\Delta H = \Delta U$, the system potential energy difference before and after crystallization occurs, as well as a more refined estimate $N_p \Delta u = \Delta H$ that takes into account α (inset, see Eq. (20)) in determining energy differences between solid and liquid particles (squares). Δu is approximately constant with T .

both $\Delta U/N_p$ and the resulting Δu . We see that the assumption of constant enthalpy difference between liquid and crystal used in deriving Eq. (6) is vindicated, and its value is approximately $\Delta H/N_p = \Delta u = 0.58$.

2. Embryo shape

As noted above, we assume that the surface area of a crystalline embryo within the droplet has surface area $S = An^{2/3}$. If we assume spherical embryos and a volume per particle to be that of an fcc particle, $v_{\text{fcc}} = 1.04$,⁵¹ we obtain $A = 4.96$. To obtain a better estimate of the shape factor, we model the embryo as an ellipsoid.^{29,30} To do this, we first compute the moment of inertia tensor for all particles in the largest embryo in the system. The eigenvalues of this tensor yield the three principal axes lengths and hence the surface area of the ellipsoid.

We plot $A = Sn^{-2/3}$ as a function of n in Fig. 6 for both critical embryos from MC (all T) and MD ($T \geq 0.410$), and all n_{max} embryos from MD trajectories for $T = 0.485$. We see that, roughly speaking, the critical embryos from different T follow the same behaviour as embryos (pre-critical, critical and post-critical) at $T = 0.485$. For large embryos (shown in the lower inset), A tends to the spherical value of ~ 5 , as is expected. For our range of T of interest (0.415–0.485), we see that the embryos become less spherical with decreasing size, and that the values of A range from about 6.7 to 8.5 (corresponding to $50 < n < 100$), with an average of 7.6. The upper inset shows that the dependence of S on $n^{2/3}$ possesses only a slowly varying departure from linearity.

3. Attachment rate

To estimate f_0 , which is essential in the prefactor in Eq. (6) and defined in Eq. (5), we follow Refs. 44 and 45. This method makes use of the fact that the change in size of a critical embryo follows a simple diffusive process since the free energy landscape is locally flat at the top of the free energy barrier.

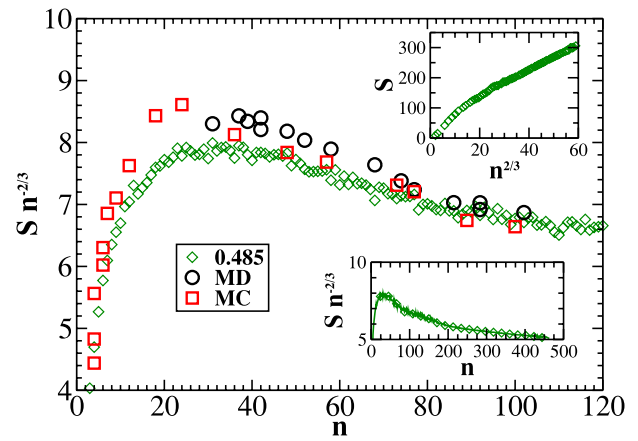


FIG. 6. Estimating the shape factor $A = Sn^{-2/3}$ as a function of embryo size, where embryo area S is that of an ellipsoid with equivalent moments of inertia as an embryo. Shown are data for critical clusters from MD ($T \geq 0.410$, circles) and MC (all T , squares), as well as from all clusters from MD simulations at $T = 0.485$. In the T range where we expect Eq. (6) to be valid, corresponding to $50 < n < 100$, A ranges from about 6.7 to 8.5. Insets show S as a function of $n^{2/3}$ (upper) and that A approaches a spherical value of 5 for large n (lower).

One defines the mean of the squared deviation from the critical size as a function of time,

$$\langle \Delta n^2(t) \rangle = \langle [n_{\text{max}}(t) - n_{\text{max}}(0)]^2 \rangle, \quad (21)$$

where $n_{\text{max}}(0) = n^*$. After a very short time, $\langle \Delta n^2(t) \rangle$ enters a diffusive regime,⁵² i.e., it becomes linear in time, and one obtains in this regime

$$f_{\text{crit}}^+ = \frac{1}{2} \text{slope of } \langle \Delta n^2(t) \rangle. \quad (22)$$

The usual process is to select a few system configurations containing an embryo of size n^* from MC simulations and to use those as starting points for MD simulations. One then selects trajectories that diffuse near n^* and averages over these trajectories, i.e., one rejects runs for which the embryo slips off the top of the barrier and shows rapid growth or decay. For low barriers, attachment of clusters of particles to the critical embryo (or break-up of a tenuously linked embryo), rather than single particle events, may contribute to rapid growth or decay. We follow the same procedure, employing from 50 (at low T) to 300 (at high T) MC configurations. The criteria for choosing what constitutes diffusive motion is unclear, for even an embryo that appears to grow rapidly first undergoes a diffusive process, and this diffusive behaviour should be included in the averaging.

To systematically explore this, we define two parameters, δ and Λ , and perform averaging in Eq. (21) for trajectories that satisfy $|n_{\text{max}}(\Lambda) - n_{\text{max}}(0)| < \delta$. In principle, δ should be of the size over which the free energy barrier is flat. Λ governs the length of time over which a trajectory ends up back within δ of n^* . A small Λ eliminates embryos that exhibit large changes in short times, while a large Λ allows embryos that grow or shrink to return to the critical region. Ideally, there should be a range of δ and Λ over which f_{crit}^+ is invariant. We note that we employ averaging over time origins, i.e., if an embryo returns to n^* after a time of 4, we treat that time as the beginning of an independent trajectory.

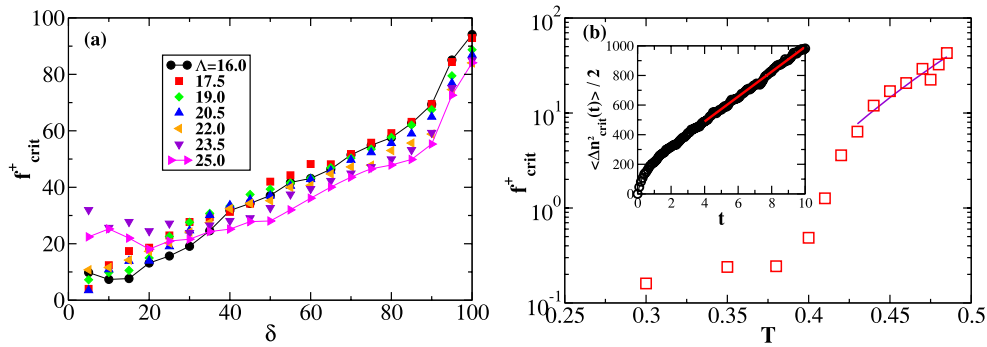


FIG. 7. Determination of the attachment rate to the critical cluster. (a) The effect of Λ and δ on f_{crit}^+ for $T = 0.485$. Short MD trajectories used to determine f_{crit}^+ contribute to the average in Eq. (21) if $|n_{\text{max}}(\Lambda) - n_{\text{max}}(0)| < \delta$. Values of Λ for the different curves are given in the legend. To obtain f_{crit}^+ , we average over all Λ and $30 \leq \delta \leq 90$. (b) f_{crit}^+ (symbols) as a function of T . Solid curve is an Arrhenius fit $\ln f_{\text{crit}}^+ = 16.4 - 6.2 \frac{1}{T}$ over $0.430 \leq T \leq 0.485$. Inset shows determination of $f_{\text{crit}}^+ = 84$ for $\delta = 100$ and $\Lambda = 25$.

The results for f_{crit}^+ as a function of δ for different Λ values for $T = 0.485$ are shown in Fig. 7(a). We see that for $\delta < 30$, there is a large spread in f_{crit}^+ over different Λ . For $\delta > 90$, there is a rapid increase in f_{crit}^+ . For δ in between, we see no obvious way to choose an optimal f_{crit}^+ , and so we average over the range $30 \leq \delta \leq 90$ over all Λ for this T to obtain $f_{\text{crit}}^+ = 43$ with a standard deviation of 13. While a value of $\delta = 90$ seems to be large, approaching n^* in fact, we note that the time over which the slope of $\langle \Delta n^2(t) \rangle$ is taken is fixed to be from 4 to 10, significantly smaller than our smallest Λ . Shown in the inset of Fig. 7(b) is $\langle \Delta n^2(t) \rangle$ for (extreme values) $\delta = 100$ and $\Lambda = 25$, and it appears to be rather well behaved, therefore not providing grounds for rejection on its own. We repeat the examination of f_{crit}^+ as a function of δ and Λ for each T . Our analysis indicates a need for a more refined way of determining f_{crit}^+ if more precise values are required.

In this way, we obtain f_{crit}^+ across our T range, which we plot in Fig. 7(b). It shows a super-Arrhenius decrease with T until an apparent falling out of equilibrium below $T = 0.4$, behavior consistent with typical glassy dynamics of simple liquids. However, as we are primarily concerned with finding γ through Eq. (6), the figure also shows a fit of f_{crit}^+ to the Arrhenius behaviour in Eq. (5) over $0.430 \leq T \leq 0.485$, with fit parameters $C = 6.2 \pm 0.3$ and $f_0 = \exp(16.4 \pm 0.7) = 1.3 \times 10^7$ (6.6×10^6 to 2.7×10^7). The marked departure below $T \approx 0.40$ from the behavior at higher T is consistent with the liquid not achieving metastable equilibrium.

4. Surface tension

Studies of crystal nucleation in bulk LJ liquid report values of $\gamma = 0.28$ to 0.30 for $T = 0.43$ and 0.45 , respectively,⁵⁰ and these compare favourably with the surface tension of a flat interface at the same T .⁵³ Using our estimates for the parameters other than γ , namely, $\Delta H = 0.58N_p$, $A = 7.6$, $f_0 = 1.3 \times 10^7$, $C = 6.2$, and the literature values of $T_m = 0.618$ ⁵⁰ and $\gamma = 0.3$,⁵⁰ we obtain $B = 2.0$ and $\lambda = 8.6 \times 10^8$. The resulting curve, according to Eq. (6), is not plotted because it fails to recover the rates in Fig. 4(a) by several orders of magnitude.

Therefore, we proceed to find γ from a one parameter fit of $J_n^+(T)$ with Eq. (6), using the above values for the

other parameters. Fitting from $T = 0.35$ to 0.485 , we obtain $\gamma = 0.13$, which is significantly lower than the bulk value. The value of γ is quite robust to how much of the data below $T = 0.40$ is used. The fit is plotted in Fig. 4(b) and models the data well down to $T = 0.385$. This validates the approximations incorporated into CNT, namely of constant ΔH , A , f_0 , C , and γ . We note that although the Arrhenius modelling of $f_{\text{crit}}^+(T)$ is valid for $T \geq 0.43$, the fit of Eq. (6) is rather good down to $T = 0.385$ for two reasons: one, the changes in $J(T)$ are driven largely by changes in $\beta\Delta G^*$ and two, the difference between the Arrhenius model and the actual values of $f_{\text{crit}}^+(T)$ between $T = 0.385$ and $T = 0.43$ is maximally of the order of a factor of five, which is compensated by a slight overestimation of $\beta\Delta G^*$ by the model. The departure of the fit from data at low T is due to the dramatic change in behavior of f_{crit}^+ below $T = 0.40$.

In Sec. IV D, we test to what extent these approximations hold in the context of $\beta\Delta G(n)$. We also test the ability of Eq. (1) to predict the rate, when $\beta\Delta G(n)$ and the other quantities in the equation are calculated through MC simulations.

D. Free energy barriers

1. $\beta\Delta G(n)$ from MC calculations

In Fig. 8, we present a sampling of the barrier profiles obtained from MC simulations. The $\beta\Delta F(n)$ curves are shifted up by $\ln N_p$ as discussed in Sec. II B and overlap well with the $\beta\Delta G(n)$ for the higher T . Parabolic fits within $\sim k_B T$ of the maxima in the curves allow us to determine Z , Z_F , $\beta\Delta G^*$, $\beta\Delta F^*$, n^* , and n_F^* .

Below $T = 0.405$, as shown in the figure for $T = 0.380$, the $\beta\Delta F(n)$ curves are monotonically decreasing. The interpretation of this results is laid out in Ref. 34 in the context of the vapour to liquid transition but still above spinodal conditions. The monotonic decrease means that for any value of n_{max} , it is more probable for n_{max} to increase in size than to decrease. Thus, the system has lost metastability and unavoidably transforms to the solid. However, the work of forming a critical embryo is still positive [$\beta\Delta G(n^*) \approx 7.6$]. So while the liquid phase is locally stable against fluctuations towards the solid state, the system as a whole is not, since it

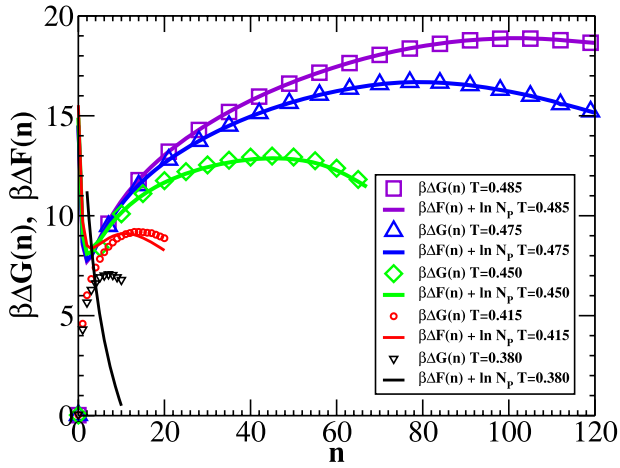


FIG. 8. Barrier profiles from umbrella sampling MC for $\beta\Delta G(n)$ (symbols) and $\beta\Delta F(n)$ (curves), which have been shifted up by $\ln N_p$ and which possess a minimum at small n . Below $T = 0.405$ (not shown), at which $\beta\Delta G^* \approx \ln N_p$, $\beta\Delta F(n)$ decreases monotonically.

is large enough to make it probable for a critical embryo to appear somewhere in the system on the time scale required for the diffusive attachment of particles.

2. T -dependence of barrier heights and critical embryo sizes, and rate prediction

The T dependence of barrier heights is shown in Fig. 9(a), while that of critical embryo size in Fig. 9(b). For the barriers, both $\Delta F^* + \ln N_p$ and ΔG^* agree quite closely. The crystallization process becomes formally driven by growth-limited nucleation when $\beta\Delta F_{\min}^* = 0$ at $T = 0.405$, at which point $\beta\Delta G^* = 7.6$. In Ref. 34, the authors gave a simple criterion for the onset of growth-limit nucleation, namely that $P_{\max}(n^*) \approx 1$, or $\beta\Delta F(n^*) = 0$, which implies $\beta\Delta G^* \approx \ln N_p = 6.40$, which is roughly $1 k_B T$ lower than what we obtain. But as this is a rule of thumb, the prediction is quite good.

Below the crossover temperature of $T = 0.405$, both $\beta\Delta G^*$ and n^* vary significantly less with decreasing T . This trend is consistent with the predictions of CNT shown in Fig. 9, especially if n^* is to remain finite as it appears to do. The crossover more or less coincides with a flattening out of the T

dependence of f_{crit}^+ , as shown in Fig. 7(b). We note that below $T = 0.405$, the equilibrium dynamics, if one could probe them, may be quite slow, and the time scale of liquid relaxation appears to be significantly longer than the time scale of embryo assembly, and thus we see an interplay between glassy dynamics and nucleation.⁵⁴ Nucleation below this temperature is occurring in an aging, non-equilibrium liquid, and this warrants further exploration.

In Fig. 9(b), we see significant differences in critical embryo size, both between n^* and n_F^* and more strikingly, between n_F^* (MC) and n_{inf}^* or n_{MEPT}^* (both MD). This is not a consequence of the definition of what constitutes a solid-like particle, but rather a real difference in the structures accessible to MD and MC in the critical region. At low T , where we are increasingly out of equilibrium, n_{inf}^* in fact increases as T decreases. Even at moderate supercooling, the critical size is larger for MD simulations.

Having calculated $\beta\Delta G(n)$, and hence obtained Z and n^* as well, we can now predict $J_{\text{CNT}}(T)$ according to Eq. (1), and we show the result in Fig. 4(b). The agreement with J_{n^*} is rather good, showing discrepancy only at $T = 0.35$ and below. Also shown in Fig. 4(b) is the kinetic prefactor Zf_{crit}^+ . Similarly to what was observed in Ref. 34 for the vapour to liquid transition, once the growth-limited nucleation regime is entered, the kinetic prefactor dictates the T dependence of the rate.

Equation (1) is the CNT prediction of the rate that lacks any thermodynamic modelling of the work of forming a critical embryo. We have already seen that modelling $\beta\Delta G(n)$ through Eq. (3) and estimating the thermodynamic quantities that enter it and Eq. (6) matches the rate from MD, but with a smaller value of γ than expected. Whatever values of γ and Δu we derive from $\beta\Delta G(n)$ as obtained from MC, from what we already know, we expect that they should combine to produce nearly equal values of $\beta\Delta G^*$ as implied from MD (since both Eqs. (1) and (6) recover the rate) and a smaller n^* . This later condition implies that we should obtain a larger value of γ . We also wish to test whether the constancy of Δu and γ obtained from MD for $T \geq 0.4$ (i.e., from the T dependence of the rate and direct calculation) is borne out in the $\Delta G(n)$ MC data.

To this end, we plot in Fig. 10(a) for $T \geq 0.4$, the quantity $2\Delta G^*/n^*$, which according to Eq. (3) should equal

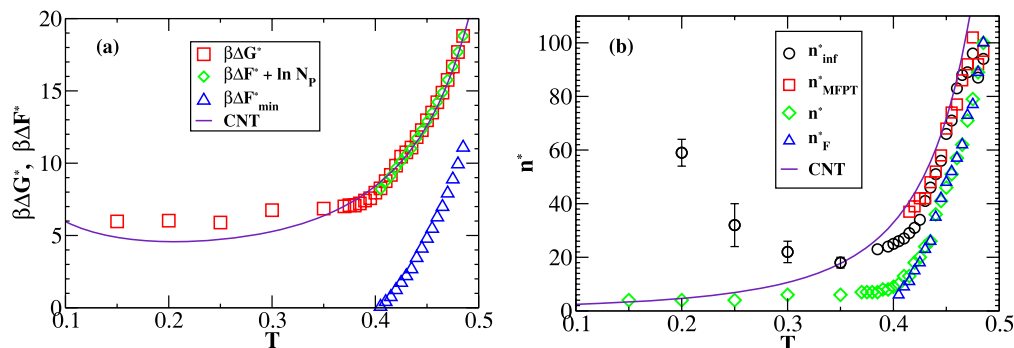


FIG. 9. (a) Nucleation barrier heights as a function of T . Solid curve shows the prediction based on CNT after obtaining only $\gamma = 0.13$ from a fit to $J(T)$ via Eq. (6). $\beta\Delta F_{\min}^* = 0$ signals the onset of growth-limited nucleation. (b) Size of the critical cluster as a function of T from various estimates. Solid curve is the CNT prediction using the same parameters as in panel (a).

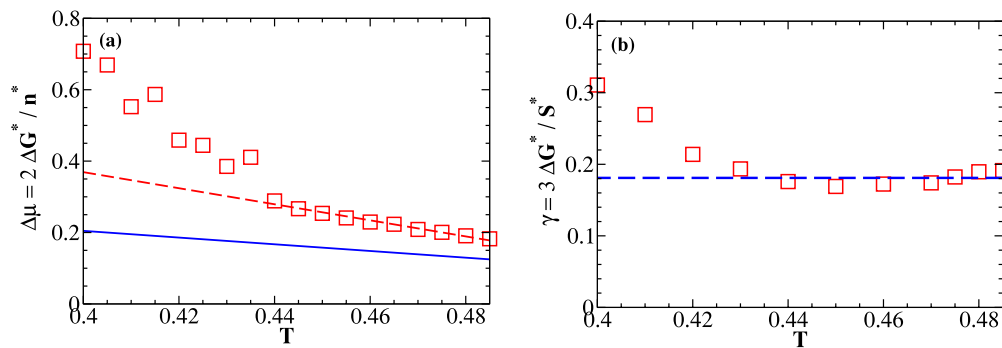


FIG. 10. Estimates of γ and $\Delta\mu$ from T dependence of MC data. Panel (a) shows the CNT relation $\Delta\mu = 2\Delta G^*/n^*$ as a function of T . Blue solid line is $\Delta\mu - \Delta uT/T_m$, setting $T_m = 0.618$ and $\Delta u = 0.58$. The dashed line is a fit (for $T \geq 0.44$), yielding $T_m = 0.564$ and $\Delta u = 1.27$. Panel (b), $\gamma = 3\Delta G^*/S^*$ versus T . Dashed line is a fit (for $T \geq 0.43$) with a constant, yielding $\gamma = 0.18$.

$\Delta\mu(T)$, which in turn should be $\Delta\mu(T) = \Delta H(1 - T/T_m)/N_p \approx \Delta u - \Delta uT/T_m$. A linear fit to data only for $T \geq 0.44$ looks convincing, and yields $T_m = 0.564$ and a value of $\Delta u = 1.27$ that is significantly higher than the independently calculated value of 0.58, roughly by a factor of 2.2. Similar discrepancies have been noted for MC studies of nucleation in Ref. 47, where across many state points the value of $\beta\Delta\mu$ obtained from fits to Eq. (3) was a factor of 2.5 higher than those calculated from thermodynamic integration, i.e., the true value.

In Fig. 10(b), we plot $\gamma = 3\Delta G^*/S^*$, which again follows from Eq. (3), where S^* is the area of the critical embryo. For a good range of data, γ is indeed constant. A fit to a constant for $T \geq 0.43$ yields $\gamma = 0.18$, which is higher than what the rate data imply but still significantly lower than the expected value of 0.3. These MC-derived values of γ , Δu , and T_m do not produce a particularly good fit to the rate when plugged in to Eq. (6).

To compare MC-derived parameters and those obtained from MD in another way, we plot, according to CNT (Eq. (3)) predictions, $\beta\Delta G^*$ from Eq. (7) in Fig. 9(a) and $n^* = 2Bk_B T_m / [\Delta u(T_m - T)^3]$ in Fig. 9(b), using parameters as obtained in Sec. IV C ($\gamma = 0.13$, $\Delta H = 0.58N_p$, and $T_m = 0.618$, giving $B = 0.16$). We find remarkably good agreement for $\beta\Delta G^*(T)$ (even for $T < 0.4$) with MC while the CNT expression for n^* gives values that are significantly higher than the MC result.

We conclude from these comparisons that the discrepancies γ and Δu between MD and MC are consistent with a larger n^* from MD, since γ from MD is smaller. However, while from MD we find that Δu is constant, MC does not show this to the same extent. Therefore, we also conclude that in order to obtain quantitative estimates from the MC-derived $\Delta G(n)$, a more nuanced modelling of $\beta\Delta G(n)$ than in Eq. (3), and a more careful definition of the surface area of embryos (including more precise definitions of liquid-like and solid-like particles) are required.

E. Escape from the critical state

We now explore the differences in n^* between MC and MFPT results that begin to be felt at $T = 0.475$. According to MFPT, $n^* \approx 100$. In Fig. 11, we plot the probability density $P(Q_6)$ for Q_6 , a global measure of the crystallinity of the system as a whole. We plot the negative of the logarithm of

the distribution in order to view it as a free energy. Generally speaking, two factors contribute to the value of Q_6 , the number of crystal-like particles and the relative orientation of crystal-like domains. For example, Q_6 will grow as the size of an fcc crystallite increases, but a large icosahedral embryo of similar size consisting of 20 fcc tetrahedra sharing a vertex will have a lower value of Q_6 .

In the first instance, we calculate $P(Q_6)$ from MD crystallization trajectories, using data up to the first time that n_{\max} reaches 100, utilizing all configurations with $60 \leq n_{\max} \leq 100$. In this way, we consider embryos in the critical region but do not allow embryos to sample states beyond the critical size. The result is a unimodal $P(Q_6)$ with a preferred value of $Q_6 = 0.1$. We refer to this value of Q_6 as *high*. If we consider embryos from all times along the trajectory, i.e., we allow the system to sample post-critical states and subsequently shrink back into the pre-critical region, the distribution changes by exhibiting a localized preference for $Q_6 = 0.04$ [a shallow minimum in $-\ln P(Q_6)$]. We refer to this value of Q_6 as *low*. Finally, we carry out MC simulations with hard wall constraints to enforce $60 \leq n_{\max} \leq 100$. The resulting free energy, also shown in Fig. 11, shows that the relative preferences for high and low Q_6 structures are similar, and that there is a free energy barrier separating the two. Thus, although there exist qualitatively different equilibrium structures in the critical region (same n_{\max} , different Q_6), MD trajectories do not easily sample the low Q_6 states until after embryos have crossed into the post-critical region. The kinetics of crossing

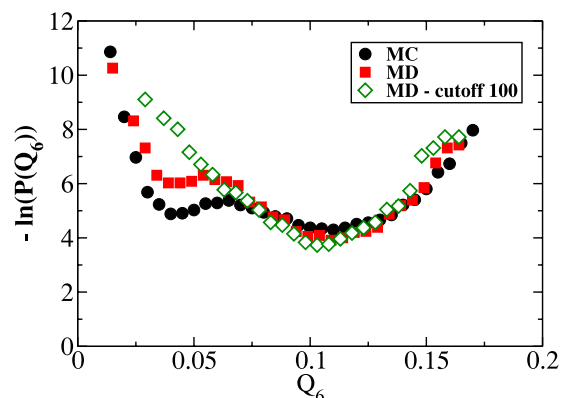


FIG. 11. Probability distributions for Q_6 at $T = 0.475$ for $60 \leq n_{\max} \leq 100$. See text for explanation.

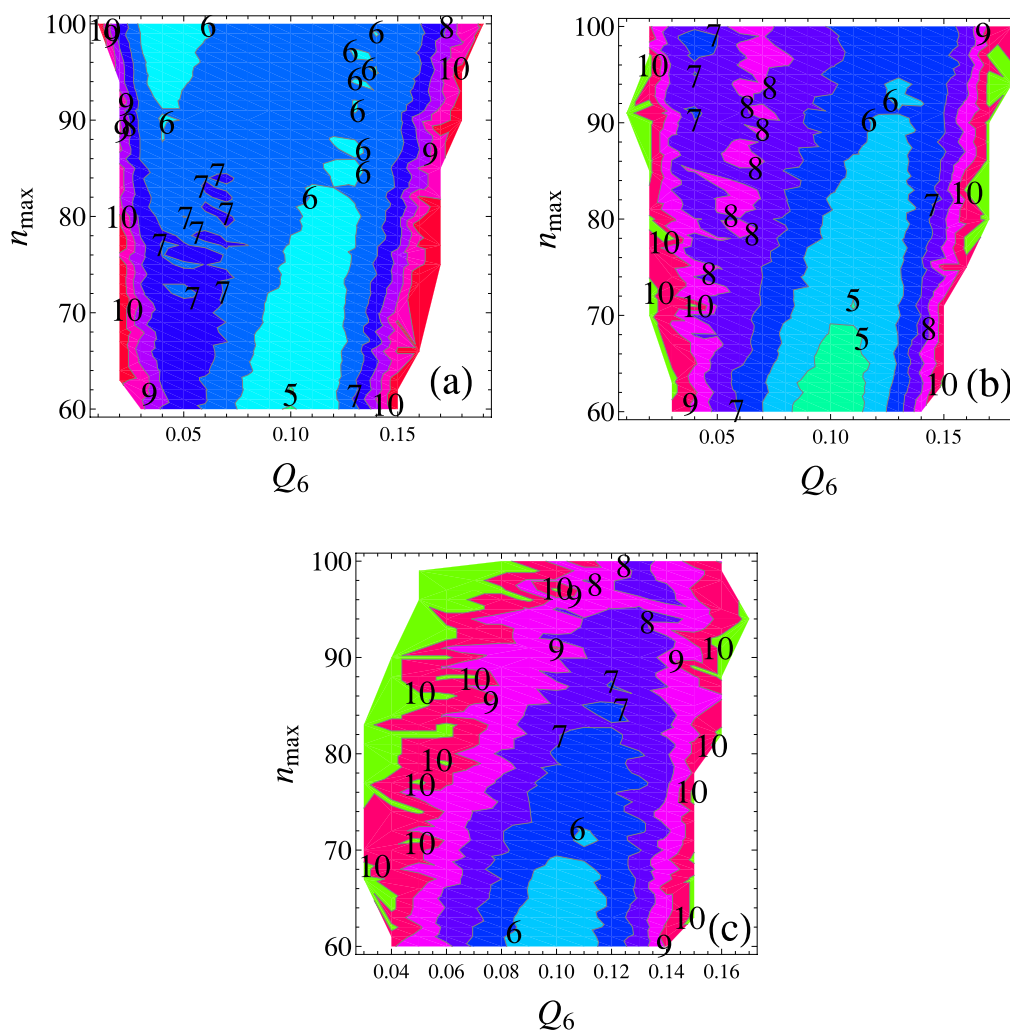


FIG. 12. Joint probability distributions for n_{\max} and Q_6 at $T = 0.475$. Plotted is $-\ln P(n_{\max}, Q_6)$ for (a) MC, (b) MD, (c) MD without allowing retracing to $n_{\max} \leq 100$. The contour lines are in increments of 1.

the small barrier for $n_{\max} \leq 100$ are apparently significantly slower than structural changes occurring for $n_{\max} > 100$.

To develop a better picture of the process, we use the data from Fig. 11 to construct two-dimensional probability distributions in both Q_6 and n_{\max} . The results are plotted in Fig. 12 as contour plots of $-\ln P(n_{\max}, Q_6)$. For the equilibrium MC data in panel (a), we see a single trough coming into the critical region from $n_{\max} = 60$ and $Q_6 = 0.1$ that becomes fairly flat at larger n_{\max} . For $n_{\max} \geq 90$, there are two exiting troughs: a weak one at high Q_6 that continues the incoming one and a more dominant one at low Q_6 . There is a small ridge separating the two troughs.

Panel (b) of Fig. 12 shows MD data where post-critical embryos that retrace back below $n_{\max} = 100$ are counted. The exiting trough at low Q_6 is higher in free energy and is much weaker than the high Q_6 exiting trough. The MD data for which no retracing is allowed, in panel (c), show only the high Q_6 exiting trough.

Thus, while it is possible for $n_{\max} < 100$ embryos to transform from high to low Q_6 , and both states have similar free energies, as the MC data show, the ridge separating high and low Q_6 prevent the MD trajectories from exploring these low Q_6 states. Further, it is clear that the critical embryo size

is significantly smaller when low Q_6 states are sampled, and this is responsible for the discrepancy between MC and MD estimates of n_{\max}^* . Another major point is that we do not see two competing pathways entering the critical region. The low Q_6 exiting trough only forms near the critical region.

While we leave a more detailed study of these transformations near the critical region for the future, we show in Fig. 13 a series of snapshots of critical configurations from $T = 0.485$ down to $T = 0.200$. For $T = 0.465$ and above, we select both high and low Q_6 specimens. We assign particle types (fcc, hcp, icosahedral) through common neighbor analysis (CNA),^{55,56} which distinguishes between local structures by considering the number of common neighbors two neighboring particles share, as well as how those common neighbors are bonded. Before carrying out the CNA analysis, we identify the particles in the largest embryo, and then carry out a conjugate gradient quench of the system to remove vibrational displacements. It is these quenched structures that are presented in Fig. 13, with particles originally in the largest embryo colour-coded, and the rest of the particles appearing in a faint shade.

While we present here only a handful of structures, the picture that emerges seems rather robust. The high Q_6 structures, Figs. 13(a), 13(c), and 13(e), appear to be stackings

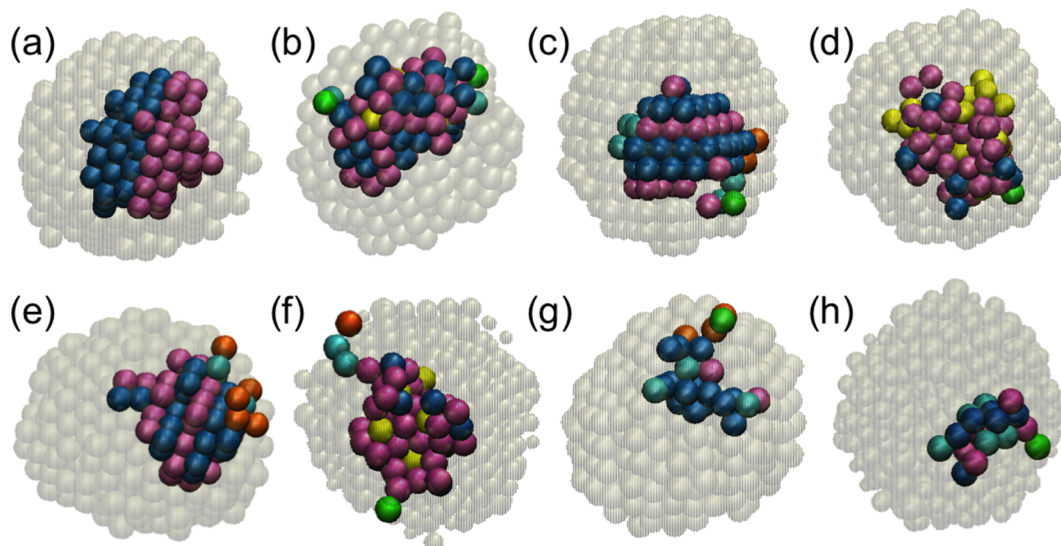


FIG. 13. Quenched droplet configurations containing embryos near critical size from (a) $T = 0.485$, $Q_6 = 0.176$, $n_{\max} = 98$, (b) $T = 0.485$, $Q_6 = 0.086$, $n_{\max} = 100$, (c) $T = 0.475$, $Q_6 = 0.129$, $n_{\max} = 79$, (d) $T = 0.475$, $Q_6 = 0.040$, $n_{\max} = 76$, (e) $T = 0.465$, $Q_6 = 0.111$, $n_{\max} = 63$, (f) $T = 0.465$, $Q_6 = 0.038$, $n_{\max} = 65$, (g) $T = 0.425$, $Q_6 = 0.078$, $n_{\max} = 24$, (h) $T = 0.200$, $Q_6 = 0.078$, $n_{\max} = 18$. The colouring scheme: blue, bulk fcc; mauve, bulk hcp; yellow, bulk icosahedral; cyan, unidentified (amorphous); green, 111 surface; orange, 100 surface; transparent tan. Note that the determination of the largest embryo is made prior to quenching and that the surface ordering visible for some of the droplets results from quenching.

of fcc and hcp layers, while the low Q_6 structures appear to be multiply twinned structures, rich in hcp, and possessing 5-fold symmetry. For the lower T shown, the embryos are small and do not show secondary organization but appear to be high in fcc. Thus, the embryos belonging to the incoming free energy trough in Fig. 12 appear to be randomly close-packed structures, while differentiation to structures suggestive of icosahedra or decahedra occurs as or after these embryos approach critical size.

The reader may notice the significant ordering apparent on the surfaces of the clusters with larger embryos shown in Fig. 13, e.g., the cluster in Fig. 13(c). This ordering results from the conjugate-gradient quench performed to enhance the ability of CNA to identify crystalline environments and was previously noted in Ref. 35. Fig. 14(a) shows the unquenched cluster at $T = 0.475$ with CNA performed on the unquenched cluster as well. In this case, there is significantly less surface ordering apparent and fewer particles within the embryo are assigned a particular classification. In Fig. 14(b), we show that calculating n_{\max} for the quenched cluster appearing

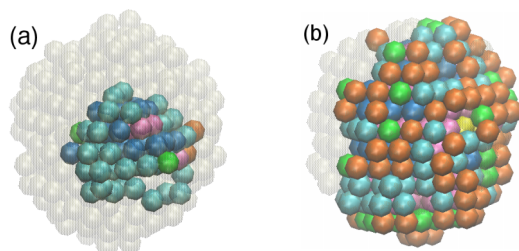


FIG. 14. Effect of conjugate-gradient quench on droplet ordering. Panel (a) shows the droplet from Fig. 13(c) prior to quenching. The surface is disordered and few particles are positively identified by CNA. Panel (b) shows the same (quenched) droplet from Fig. 13(c) but with the determination of n_{\max} done after quenching. Quenching induces significant ordering. Color scheme is the same as in Fig. 13.

in Fig. 13(c) results in many more solid-like particles, particularly on the surface. Thus, quenching presents a trade-off: it enhances identification of crystalline types but induces significant ordering around embryos. The significant ordering induced by quenching is certainly interesting and is consistent with the “prestructured surface cloud” around crystallites pointed out in Ref. 58.

V. DISCUSSION

Part of the motivation for this work comes from previous studies on the interpretation of $\beta\Delta F_{\min}^*$ approaching zero, its relation to nucleation rates and liquid metastability, and the appropriateness of using the largest embryo in the system as an order parameter. While previous work misidentified this barrier disappearance as a condition for a spinodal (and the refutation of this pointed out its size dependence),⁵⁷ it clearly signalled some sort of limit to metastability. The recent scenario laid out in Ref. 34, namely that it signals unavoidable crystallization achieved through growth-limited nucleation, is supported by our work. We add that in our case, growth-limited nucleation proceeds in an out-of-equilibrium liquid. By growth-limited nucleation, we mean that with near certainty, somewhere in the system, a critical nucleus will form through $\sim n^*$ consecutive particle additions, and so crystallization is controlled by the rate at which liquid-like particles attach themselves to crystal-like ones. This is what we see when we predict the rate through Eq. (1), which matches MD rate determination for almost the entire range of T , as seen in Fig. 4(b). This growth-controlled nucleation mechanism, the onset of which is determined in part by the size of the system, is likely important in crystallization occurring in other liquid droplet systems.^{59,60}

For our LJ clusters, where nucleation originates within the bulk, CNT as formulated for homogeneous nucleation for

bulk liquids works quite well. We see that a controlling factor, despite the presence of the surface, is the temperature T_m at which $\Delta\mu = 0$ in bulk systems, even though in our finite-sized system the coexistence temperature T_m^c is significantly lower.

We find that the simple modelling often used in CNT, such as constant γ , ΔH , and A , and Arrhenius temperature dependence of f_{crit}^+ is supported by our results in independently determining these quantities, at least for moderate supercooling. Using these quantities as calculated allows us to fit the rate with a single value of $\gamma = 0.13$ convincingly well over a broad range of T . There is very good consistency between thermodynamics and rates, at least for $T \geq 0.40$. There is some ambiguity regarding the values of ΔH , or rather $\Delta\mu$, and γ when using the CNT model in Eq. (3) to compare independently calculated $\beta\Delta G(n)$, as the $\beta\Delta G(n)$ curves yield different values of $\Delta\mu$, and γ . This points to the need for more detailed modelling of $\beta\Delta G(n)$.^{43,61}

The temperature $T_x = 0.405$ at which system metastability is lost and growth-limited nucleation sets in is well approximated by the condition $\beta\Delta G^* = \ln N_p$.³⁴ Near this same T_x , f_{crit}^+ begins a rather strong departure from higher T behavior by becoming roughly constant. This may indicate the liquid's inability to equilibrate because of sluggish dynamics, but may be at least partially driven by the weak T dependence of n^* that sets in below T_x . That the system as a liquid does not reach metastable equilibrium is indicated by the potential energy time series at low T . The ability for the liquid to undergo significant diffusive motion (enough to form critical embryos) while not equilibrating itself may be due to a decoupling of diffusive and collective relaxation time scales characteristic of glassy dynamics.⁵⁴ It is slightly curious that the onset of glassy dynamics should coincide with the system size dependent T_x .

As for the MC simulations, the constraint should allow for equilibration to occur since the size of the largest embryo is constrained. It is perhaps likely that relaxation of the metastable liquid requires significantly longer times than our MC of 500 000 iterations (5×10^6 displacement attempts per particle). Questions about the relaxation of the liquid surrounding embryos are perhaps more easily addressed in bulk systems, where determining the dynamics of the system is somewhat more straightforward in the absence of a surface. While the increase in n_{inf} that we see at low T may be viewed positively for the case of the spinodal scenario, the difficulties in discerning critical embryos precisely and questions regarding equilibrium must be carefully addressed. Nonetheless, it is remarkable and slightly curious that the (more) equilibrated MC simulations at low T should predict the rate so well through Eq. (1) when there is such a large difference in n^* when comparing MD and MC.

Commenting on early work,³⁵ where the free energy was calculated as a function of Q_6 -based measures of the bulk and surface crystallinity, at $T = 0.475$, the barrier separating the liquid from a low Q_6 5-fold structure was $0.5k_B T$ or less (as calculated by subtracting from the free energy of the saddle point the minimum value in the liquid basin), implying that the system as a liquid had (practically) lost stability at this T . However, here we see that at $T = 0.475$, $\beta\Delta F^* = 10$, which is considerably higher. Thus, care must be taken when gauging phase stability from free energies based on Q_6 , as there are

crystal-like states with values of Q_6 that overlap with those of the liquid.

In terms of structural differentiation that occurs in cluster crystallization, the picture that emerges in our work is that pre-critical nuclei are layered hcp-fcc planes, but that (at least) two types of structures, with different Q_6 values, leave the critical region. A small barrier in Q_6 appears to separate the two, thus preventing MD simulations from sampling the low Q_6 states with twinned, five-fold structure until the embryo exceeds the critical size. It seems that small icosahedral nuclei are unfavourable, an observation that may find support in studies of small isolated LJ clusters.¹³ The lack of sampling of low Q_6 critical states leads to disparity in determining n^* in MD and MC, and will make it more difficult to use the MFPT formalism to reconstruct the free energy landscape. As nucleation studied here occurs within the bulk of the cluster, perhaps a similar scenario occurs in bulk LJ. We look forward to exploring these issues in more detail in the future.

VI. CONCLUSIONS

We determine the rate of nucleation in a cluster of 600 LJ particles through MD simulations by calculating mean first-passage times of embryo sizes. For several orders of magnitude, the rate follows expectations from CNT under the simplest of assumptions, namely a constant (ellipsoidal) shape of crystallites, a constant enthalpy difference, Arrhenius dependence of the attachment rate, a melting temperature following from the bulk, and a constant surface tension. Treating the surface tension as a fitting parameter to the rate while independently determining the other quantities results in excellent agreement from $T = 0.485$ down to $T \approx 0.40$ of the temperature dependence of the rate with CNT and of the work of forming critical nuclei with MC simulations. However, the value of the effective surface tension $\gamma = 0.13$ is smaller than expected.

Near $T_x = 0.4$, the rate starts approaching a maximum as the system loses its ability to maintain metastability. This is evidenced by a monotonically decreasing free energy that has as its argument the size of the largest embryo in the system. At and below this temperature, crystallization proceeds through growth-limited nucleation in an unequilibrated liquid. The liquid phase is not inherently unstable itself, as there is a finite work required to form critical nuclei, but rather the barrier has become sufficiently small, as determined approximately by $\beta\Delta G^* = \ln N_p$. This picture follows what was observed for the vapour-liquid transition.³⁴

Surprisingly robust are the excellent predictions of the rate from MC-based calculations of $\beta\Delta G^*$, Z , and f_{crit}^+ . The predictions match the rate excellently above and below T_x . Above T_x , the free energy $\beta\Delta F(n_{\text{max}})$ gives the same barrier heights as $\beta\Delta G(n)$, given proper normalization.

For our system, MD and MC show discrepancies in n_F^* , even at slight to moderate supercooling, because of the appearance of embryos with twinned structures exhibiting 5-fold symmetry. The differentiation between these and hcp-fcc stacked structures happens only in the critical region; pre-critical nuclei do not seem to possess the 5-fold symmetry of the icosahedral structures to which LJ clusters often freeze.

TABLE I. Simulation results data. For $\beta\Delta F^*$, we have added $\ln N_p = \ln 600 = 6.40$ in order to better compare with $\beta\Delta G^*$. For example, at $T = 0.485$, the bare value of $\beta\Delta F^* = 12.40$ and at $T = 0.410$, the bare value of $\beta\Delta F^* = 2.31$.

T	$\beta\Delta G^*$	$\beta\Delta F^*$	$\beta\Delta F_{\min}^*$	n^*	n_F^*	n_{inf}^*	Z	f_{crit}^+	S^*	$J_n^* \times 10^5$
0.485	18.80	18.80	11.08	100	100	94	0.0167	42.81	143.08	0.22
0.480	17.69	17.69	9.93	89	89	87	0.0172	32.45	134.40	0.66
0.475	16.69	16.69	8.89	79	77	96	0.0216	22.43	130.42	1.89
0.470	15.76	15.76	7.92	71	73	89	0.0219	29.18	127.70	4.08
0.465	14.88	14.88	6.99	62	62	88				7.75
0.460	14.21	14.22	6.26	57	57	83	0.0249	20.67	113.82	15.87
0.455	13.50	13.5	5.47	51	52	71				32.67
0.450	12.97	12.89	4.79	46	48	66	0.0249	16.99	103.53	56.35
0.445	12.29	12.29	4.10	41	42	56				98.86
0.440	11.81	11.73	3.45	36	35	51	0.0256	11.96	88.61	149.73
0.435	11.08	11.01	2.91	26	26	46				227.71
0.430	10.75	10.60	2.31	24	23	41	0.0445	6.37	71.65	337.16
0.425	10.45	10.13	1.65	20	18	34				486.30
0.420	9.83	9.67	1.14	18	15	31	0.0553	3.59	57.91	647.61
0.415	9.19	9.11	0.74	13	11	29				791.17
0.410	8.76	8.71	0.46	13	9	27	0.0825	1.26	39.98	941.44
0.405	8.26	8.20	0.14	10	7	26				1038.43
0.400	7.96			9		25	0.1128	0.49	30.74	1275.26
0.395	7.58			8		24				1366.98
0.390	7.42			8						
0.385	7.22			7		23				1580.74
0.380	7.07			7			0.1392	0.24	25.09	
0.375	7.09			7						
0.370	7.01			7						
0.350	6.86			6		18	0.1370	0.24	19.88	2705.77
0.300	6.75			6		22	0.1350	0.16	20.81	2875.35
0.250	5.90			4		32			12.17	1873.84
0.200	6.03			4		59			14.02	734.11
0.150	5.97			4					11.19	

In the critical region, there appears to be a small free energy barrier with Q_6 as an order parameter between the hcp-fcc and 5-fold structures, inhibiting MD trajectories from sampling the same structures accessible to constrained MC simulations.

ACKNOWLEDGMENTS

We thank Richard K. Bowles, Peter H. Poole, Sergey V. Buldyrev, and especially David Reguera for warm and enlightening discussions. We thank Natural Sciences and Engineering Research Council (Canada) for funding. Computational facilities are provided by ACEnet, a member of Compute Canada and the regional high performance computing consortium for universities in Atlantic Canada. ACEnet is funded by the Canada Foundation for Innovation (CFI), the Atlantic Canada Opportunities Agency (ACOA), and the provinces of Newfoundland and Labrador, Nova Scotia, and New Brunswick.

APPENDIX: TABULATED SIMULATION RESULTS

We list detailed results in Table I: Barrier heights, $\beta\Delta G^*$ from MC, $\beta\Delta F^*$ from MC, and $\beta\Delta F_{\min}^*$ from MC; critical sizes, n^* from MC, n_F^* from MC, and n_{inf}^* from MD; Zeldovich factor Z from MC; attachment rate f_{crit}^+ based on embryos taken from

MC; surface area S^* of critical embryos taken from MC; and nucleation rate J_n^* from MFPT data.

¹A. Puzder, A. J. Williamson, J. C. Grossman, and G. Galli, *J. Chem. Phys.* **117**, 6721 (2002).

²F. Iori and S. Ossicini, *Phys. E* **41**, 939 (2009).

³T. Shimizu-Iwayama, N. Kurumado, D. E. Hole, and P. D. Townsend, *J. Appl. Phys.* **83**, 6018 (1998).

⁴W. Kruppa, M. G. Ancona, R. W. Rendell, A. W. Snow, E. E. Foos, and R. Bass, *Appl. Phys. Lett.* **88**, 053120 (2006).

⁵V. Venkatesh, A. Shukla, S. Sivakumar, and S. Verma, *ACS Appl. Mater. Interfaces* **6**, 2185 (2014).

⁶A. Visikovskiy, K. Mitsuhashi, and Y. Kido, *J. Vac. Sci. Technol., A* **31**, 061404 (2013).

⁷K. Mitsuhashi, M. Tagami, T. Matsuda, A. Visikovskiy, M. Takizawa, and Y. Kido, *J. Chem. Phys.* **139**, 124303 (2012).

⁸M. Penza, G. Cassano, R. Rossi, M. Alvisi, A. Rizzo, M. A. Signore, Th. Dikonimos, E. Serra, and R. Giorgi, *Appl. Phys. Lett.* **90**, 173123 (2007).

⁹F. Baletto and R. Ferrando, *Rev. Mod. Phys.* **77**, 371 (2005).

¹⁰J. Farges, M. F. de Feraudy, B. Raoult, and G. Torchet, *J. Chem. Phys.* **112**, 5067 (1983).

¹¹J. Farges, M. F. de Feraudy, B. Raoult, and G. Torchet, *J. Chem. Phys.* **84**, 3491 (1986).

¹²B. Raoult, J. Farges, M. F. de Feraudy, and G. Torchet, *Philos. Mag. B* **60**, 881 (1989).

¹³D. J. Wales and J. P. K. Doye, *J. Phys. Chem. A* **101**, 5111 (1997).

¹⁴D. J. Wales, *Energy Landscapes with Applications to Clusters, Biomolecules and Glasses* (Cambridge University Press, Cambridge, 2003).

¹⁵J. P. K. Doye, M. A. Miller, and D. J. Wales, *J. Chem. Phys.* **110**, 6896 (1999).

¹⁶W. Polak and A. Patrykiewicz, *Phys. Rev. B* **67**, 115402 (2003).

¹⁷Y. Xiang, L. Cheng, W. Cai, and X. Shao, *J. Chem. Phys.* **108**, 9516 (2004).

¹⁸W. Polak, *Eur. Phys. J. D* **40**, 231 (2006).

- ¹⁹E. G. Noya and J. P. K. Doye, *J. Chem. Phys.* **124**, 104503 (2006).
- ²⁰V. A. Mandelshtam and P. A. Frantsuzov, *J. Chem. Phys.* **124**, 204511 (2006).
- ²¹W. Polak, *Phys. Rev. E* **77**, 031404 (2008).
- ²²W. Polak, *Eur. Phys. J. D* **67**, 74 (2013).
- ²³W. Polak, *Comput. Theor. Chem.* **1021**, 268 (2013).
- ²⁴W. Polak, *J. Cryst. Growth* **401**, 44 (2014).
- ²⁵P. G. Debenedetti, *Metastable Liquids. Concepts and Principles* (Princeton University Press, Princeton, 1996).
- ²⁶C. C. Asuquo and R. K. Bowles, *J. Chem. Phys.* **116**, 14619 (2012).
- ²⁷E. Mendez-Villuendas, I. Saika-Voivod, and R. K. Bowles, *J. Chem. Phys.* **127**, 154703 (2007).
- ²⁸J. W. Cahn and J. E. Hilliard, *J. Chem. Phys.* **31**, 688 (1959); W. Klein and F. Leyvraz, *Phys. Rev. Lett.* **57**, 2845 (1986); J.-x. Yang, H. Gould, and W. Klein, *ibid.* **60**, 2665 (1988).
- ²⁹F. Trudu, D. Donadio, and M. Parrinello, *Phys. Rev. Lett.* **97**, 105701 (2006).
- ³⁰H. Wang, H. Gould, and W. Klein, *Phys. Rev. E* **76**, 031604 (2007).
- ³¹L. S. Bartell and D. T. Wu, *J. Chem. Phys.* **127**, 174507 (2007).
- ³²J. Wedekind, R. Strey, and D. Reguera, *J. Chem. Phys.* **126**, 134103 (2007).
- ³³J. Wedekind and D. Reguera, *J. Phys. Chem. B* **112**, 11060 (2008).
- ³⁴J. Wedekind, G. Chkonia, J. Wolk, R. Strey, and D. Reguera, *J. Chem. Phys.* **131**, 114506 (2009).
- ³⁵I. Saika-Voivod, L. Poon, and R. K. Bowles, *J. Chem. Phys.* **133**, 074503 (2010).
- ³⁶E. Mendez-Villuendas and R. K. Bowles, *Phys. Rev. Lett.* **98**, 185503 (2007).
- ³⁷S. P. Das, *Statistical Physics of Liquids at Freezing and Beyond* (Cambridge University Press, New York, 2011).
- ³⁸N. Okui, *J. Mater. Sci.* **25**, 1623 (1990).
- ³⁹E. Clouet, in *ASM Handbook* (ASM International, 2009), Vol. 22A, p. 203.
- ⁴⁰B. Scheifele, I. Saika-Voivod, R. K. Bowles, and P. H. Poole, *Phys. Rev. E* **87**, 042407 (2013).
- ⁴¹P. Hanggi, P. Talkner, and M. Borkovec, *Rev. Mod. Phys.* **62**, 251 (1990).
- ⁴²H. J. C. Berendsen, D. van der Spoel, and R. van Druren, *Comput. Phys. Commun.* **91**, 43 (1995); E. Lindahl, B. Hess, and D. van der Spoel, *J. Mol. Model.* **7**, 306 (2001), online at <http://link.springer.com/article/10.1007/s008940100045>; D. van der Spoel, E. Lindahl, B. Hess, G. Groenhof, A. E. Mark, and H. J. C. Berendsen, *J. Comput. Chem.* **26**, 1701 (2005); B. Hess, C. Kutzner, D. van der Spoel, and E. Lindahl, *J. Chem. Theory Comput.* **4**, 435 (2008).
- ⁴³S. Lundrigan and I. Saika-Voivod, *J. Chem. Phys.* **131**, 104503 (2009).
- ⁴⁴S. Auer and D. Frenkel, *J. Chem. Phys.* **120**, 3015 (2004).
- ⁴⁵C. Valeriani, E. Sanz, and D. Frenkel, *J. Chem. Phys.* **122**, 194501 (2005).
- ⁴⁶P. J. Steinhardt, D. R. Nelson, and M. Ronchetti, *Phys. Rev. B* **28**, 784 (2001).
- ⁴⁷I. Saika-Voivod, F. Romano, and F. Sciortino, *J. Chem. Phys.* **135**, 124506 (2011).
- ⁴⁸P. R. ten Wolde, M. J. Ruiz-Montero, and D. Frenkel, *J. Chem. Phys.* **104**, 9932 (1996).
- ⁴⁹M. R. Shirts and J. D. Chodera, *J. Chem. Phys.* **129**, 124105 (2008). We use the “pymbar-2.0beta” implementation of the MBAR method available from <https://simtk.org/home/pymbar>.
- ⁵⁰V. G. Baidakov and A. O. Tipsev, *J. Chem. Phys.* **136**, 074510 (2012).
- ⁵¹E. A. Mastny and J. J. de Pablo, *J. Chem. Phys.* **127**, 104504 (2007).
- ⁵²I. Saika-Voivod, P. H. Poole, and R. K. Bowles, *J. Chem. Phys.* **124**, 224709 (2006).
- ⁵³V. G. Baidakov, A. O. Tipsev, K. S. Bobrov, and G. V. Ionov, *J. Chem. Phys.* **132**, 234505 (2010).
- ⁵⁴I. Saika-Voivod, R. K. Bowles, and P. H. Poole, *Phys. Rev. Lett.* **103**, 225701 (2009).
- ⁵⁵A. S. Clarke and H. Jonsson, *Phys. Rev. E* **47**, 3975 (1993).
- ⁵⁶S. C. Hendy and B. D. Hall, *Phys. Rev. B* **64**, 085425 (2001).
- ⁵⁷P. Bhimalapuram, S. Chakrabarty, and B. Bagchi, *Phys. Rev. Lett.* **98**, 206104 (2007); L. Maibaum, “Comment,” *ibid.* **101**, 019601 (2008); P. Bhimalapuram, S. Chakrabarty, and B. Bagchi, “Reply,” *ibid.* **101**, 019601 (2008).
- ⁵⁸W. Lechner, C. Dellago, and P. G. Bolhuis, *Phys. Rev. Lett.* **106**, 085701 (2011).
- ⁵⁹L. M. Xu, S. V. Buldyrev, H. E. Stanley, and G. Franzese, *Phys. Rev. Lett.* **109**, 095702 (2012).
- ⁶⁰J. A. Sellberg, C. Huang, T. A. McQueen, N. D. Loh, H. Laksmono, D. Schlesinger, R. G. Sierra, D. Nordlund, C. Y. Hampton, D. Starodub, D. P. DePonte, M. Beye, C. Chen, A. V. Martin, A. Barty, K. T. Wikfeldt, T. M. Weiss, C. Caronna, J. Feldkamp, L. B. Skinner, M. M. Seibert, M. Messerschmidt, G. J. Williams, S. Boutet, L. G. M. Pettersson, M. J. Bogan, and A. Nilsson, *Nature* **510**, 381 (2014).
- ⁶¹J. Russo, F. Romano, and H. Tanaka, *Nat. Mater.* **13**, 733 (2014).